Study of focused-ion-beam–induced structural and compositional modifications in nanoscale bilayer systems by combined grazing incidence x ray reflectivity and fluorescence

Erhan Arac,[1,a)] David M. Burn,[1] David S. Eastwood,[1] Thomas P. A. Hase,[2] and Del Atkinson[1]
[1]*Department of Physics, Durham University, Durham DH1 3LE, United Kingdom*
[2]*Department of Physics, University of Warwick, Coventry CV4 7AL, United Kingdom*

(Received 8 November 2011; accepted 19 January 2012; published online 28 February 2012)

A detailed analysis of the structural and compositional changes in NiFe/Au bilayers induced by a focused ion beam (FIB) is presented. NiFe/Au bilayers with different thickness were irradiated with a focused 30 keV Ga^+ ion beam, and the evaluation of the individual layers and interfaces were investigated systematically as a function of a broad range of irradiation fluence using grazing incidence x ray reflectivity (GIXRR) and angular dependent x ray fluorescence (ADXRF) techniques carried out at synchrotron radiation sources. Experimental data were collected from 1.3 mm × 4.5 mm structures, and irradiation of such a broad areas with a 100-nm-wide focused ion beam is a challenging task. Two irradiation regimes were identified: For Ga^+ fluences $< 15.6 \times 10^{14}$ ion/cm^2 (low dose regime), the main influence of the focused ion beam is on the interface and, beyond this dose (high dose regime), sputtering effects and ion implantation becomes significant, eventually causing amorphization of the bilayer system. The broadening of the NiFe/Au interface occurs even at the lowest dose, and above a critical fluence ($\Phi = 1.56 \times 10^{14}$ ion/cm^2) can be represented by an interfacial-intermixed layer ($Ni_xFe_yAu_{(1-x-y)}$; $x = 0.5$-0.6, $y = 0.1$-0.15) formed between the NiFe and Au layers. The thickness of this layer increases with irradiation fluence in the low dose regime. A linear relationship is found between the squared intermixing length and irradiation fluence, indicating that FIB-induced mixing is diffusion controlled. The ballistic model fails to describe FIB-induced intermixing, indicating that thermodynamical factors, which might be originated from FIB specific features, should be taken into account. Despite the complexity of the chemical and structural formation, good agreement between the experiment and theory highlights the functionality of the combined GIXRR and ADXRF techniques for studying intermixing in high resolution. © *2012 American Institute of Physics*. [http://dx.doi.org/10.1063/1.3689016]

I. INTRODUCTION

Nanoscale fabrication and local modification of functional behavior are highly sought after for applications in semiconductor and spintronic device technologies. A focused ion beam (FIB) with a beam diameter ranging from a few μm to 10 nm has become a versatile tool for direct lithographic patterning and for modifying properties locally. It can be used as a dry etching technique and has been applied to create high quality planar nanostructures and data storage elements.[1–3] Also, it has been applied to nanopatterning of optoelectronic devices, ferroelectric capacitors, alumina nanochannels, as well as electrically conducting connections.[4–7] It has been used to modify and tune the local magnetic properties in magnetic systems.[8–12] This approach has been used to realize artificial domain structures[13] and locally control the domain wall dynamics.[14] In spite of the enormous wealth of FIB applications, there are few studies concerned with the details of the physical process manifest within the materials during FIB exposure.[11,15–17]

There is a great amount of work done on mechanism of ion beam irradiation and intermixing using ion implanters and accelerators as ion sources. There were early works aimed to modify the magnetic properties of various systems.[18,19] The pioneering work of Chappert *et al.*[20] on the Co/Pt magnetic systems stimulated numerous studies focused on the influence of the ion irradiation and implantation on the perpendicular magnetic anisotropy (PMA) systems.[21–36] In-plane magnetic systems, such as Permalloy (nominal composition $Ni_{80}Fe_{20}$), have also attracted interest, and some similar studies have been conducted on those systems.[37–39]

Energy transfer from the incident ions can cause atomic displacements of target atoms, leading to intermixing across the interface. The re-arrangement of intermixed atoms initially located around the interfaces may induce alloy formation,[23,28,36,40,41] changes in grain size,[42] and lattice expansion due to local stress relaxation. Amorphisation, sputtering, and total destruction of the crystalline phase ultimately occur at higher doses.[37,39]

The basic physics behind ion irradiation–induced changes of magnetic properties using accelerators and ion

a)Electronic mail: erhan.arac@durham.ac.uk.

implanters is somewhat established and agreed upon. However, the mechanism can be different in the case of FIB irradiation, because of its specific features, such as very localized dosing, highly localized kinetic energy, heat-matter deposition, and fast rastering scan.

Here, we present a detailed experimental work that aims to understand the structural and compositional modifications induced by focused ion beam irradiation in nanoscale bilayer systems as a function of both FIB fluence and the layer thicknesses in the bilayer. One of the main challenges in designing such an experiment is to irradiate large areas with a focused ion beam, which is necessary to average experimental data over large regions of interest. We collected experimental data from 7.15 mm^2 regions irradiated with ion beam of 102 nm in diameter. Ion beam irradiation was undertaken with 30 keV Ga^+ ions using a dual beam FIB system. Further scientific value and novelty lie in the combined application of grazing incidence x ray reflectivity (GIXRR) and angular dependent x ray fluorescence (ADXRF) techniques to study structural and compositional changes. The combined GIXRR and ADXRF analysis ensures accurate interface width and layer composition. To our knowledge, they were not applied to any FIB-irradiated system to study microstructural details.

The NiFe/Au system was selected as a model for this study for several reasons. Gold is commonly used as a protective cap on thin-film materials to limit oxidation, and being chemically unreactive, the physical effects of FIB irradiation are unlikely to be complicated by the formation of additional chemical phases resulting from the ion-induced interactions with atoms in the adjacent layer. This is the case for the transition metal ferromagnets and their alloys, of which $Ni_{80}Fe_{20}$ is the archetypal material used in numerous studies of thin-films and nanostructures with in-plane magnetization. Furthermore, the large electron density contrast between the period 6 (Au) and period 4 (Ni/Fe) elements and the well-separated fluorescence emission lines makes this bilayer system well suited for a structural investigation using grazing incidence x ray reflectivity and the fluorescence measurements. This study is, therefore, directly relevant to understanding FIB-induced structural changes in the NiFe/Au magnetic bilayer system and is more widely applicable to a general understanding of the structural modifications resulting from ion irradiation of nanoscale bilayer systems.

II. EXPERIMENTAL

NiFe/Au bilayers test structures were prepared by thermal evaporation through a shadow mask onto a thermally oxidized Si substrate. The NiFe was evaporated from a single alloy source of composition $Ni_{81}Fe_{19}$. Wave-length dispersive x ray measurements (WDS) have shown that the composition of such evaporated films is close to that of the alloy source, but can show a slightly increase in the nickel content.[43] The base pressure of the vacuum system was 5×10^{-7} Torr, and during deposition, the pressure ranged between 1×10^{-6} and 4×10^{-6} Torr. The two layers were deposited in succession without breaking vacuum at rates of 0.6 Å/s for the NiFe and 0.3 Å/s for the gold. The nominal thickness and deposition rate were monitored using an *in situ* quartz crystal rate monitor, which was calibrated previously using in-house x ray reflectivity measurements. A range of bi-layers were grown with varying Au and NiFe layer thicknesses. In this paper, detailed results of the effect of FIB fluence are described for a bilayer with nominal thicknesses NiFe (20 nm) and Au (2.5 nm). This combination of relatively thin top layer and thick under-layer was selected, as the top layer is sufficiently thin to allow intermixing effects at low doses, but is not significantly affected by sputtering loss at low doses. In addition, the thick under-layer presents the opportunity to track the progressive spread of atoms from the top layer deeper into the under-layer. In addition, results are also presented from a bilayer combination of NiFe (10 nm)/Au (6 nm). This second series of samples allows the effects of the top layer thickness on the intermixing process to be investigated.

For each bilayer thickness combination studied, a series of parallel test structures were created by deposition through a multi-aperture shadow mask onto a single substrate. This created several identical bilayer structures that were independently subjected to FIB irradiation and measurement. The individual test structures were 1.3-mm-wide and 5.5-mm-long and separated from neighboring structures by 1 mm. The relatively large area of the structures was needed to match the footprint of the x ray beam, which has a width of the order of 200 μm and was elongated to several millimeters along the sample surface at grazing incidence. The individual structures were irradiated with Ga^+ ions using a focused ion beam system (FEI Helios NanoLab 600). In order to achieve the irradiation of such relatively large areas, the focused beam was raster scanned over 100 μm square write fields. The sample stage was moved between consecutive write fields to irradiate an entire test structure. The stitching error associated with the stage movements was at worst 1 μm, which is negligible compared to the footprint of the x ray beam. The test structures of the series A bilayer (NiFe (20 nm)/Au (2.5 nm)) were irradiated with fluences, Φ, ranging from 1.56×10^{14} ion/cm^2 to 48.6×10^{14} ion/cm^2, with one structure remaining unirradiated. The test structures of the second bilayer NiFe (10 nm)/Au (6 nm) (series B) were irradiated with $1.56 \times 10^{14} \leq \Phi \leq 7.1 \times 10^{14}$ ion/cm^2. Details of the samples and doses are presented in Table I. The Ga^+ ion irradiation was conducted at normal incidence to the sample surface with an incident ion energy of 30 keV and a beam current of 6.7 nA. A 50% overlap was set between adjacent pixels, resulting in an effective beam diameter of 102 nm. The ion fluence was controlled by repeated exposures of each pixel for a set dwell time of 1 μs.

Structural and compositional analysis was based on a combination of grazing incidence x ray reflectivity (GIXRR) and angular dependent x ray fluorescence (ADXRF). The combination of these techniques provides a constructive set of data used to study the chemical and structural changes with nm resolution, something that is lacking in conventional methods, such as Rutherford back scattering (RBS) and secondary ion mass spectroscopy (SIMS). Reflectivity allows the layer thickness and inter-facial roughness to be quantified. The scattered intensity is proportional to the Fourier transform of the effective electron density profile. Variations

TABLE I. Details of the samples measured. Nominal thicknesses for each series of samples are shown in the left column. Sample identifiers with corresponding doses are presented for each series. (Au thickness for the unirradiated structure 4B is 7.0 nm).

Thickness NiFe/Au (nm)	# Structure	Fluence ($\times 10^{14}$ ion/cm^2)
20/2.5	1A	unirradiated
	2A	1.56
	3A	3.12
	4A	6.24
	5A	7.8
	6A	15.6
	7A	31.2
	8A	46.8
10/6	1B	unirradiated
	2B	1.56
	3B	4.58
	4B	7.1

in the electron density profile can be related to changes in material density, but also reflect the intermixing of atomic species at the interface, indicating compositional changes. Chemical compositional information that is complementary to the reflectivity data can be extracted from ADXRF studies. By monitoring the fluorescent yield as a function of incidence angle, the depth profile of the elemental composition can be determined, making it possible to track the displacements of the different atomic species.

The GIXRR measurements were performed on the BM28 XMaS beamline at the ESRF and on the X22 C beamline at the NSLS using 11.8 keV, 10 keV, and 12.5 keV x ray energies. The test structures were located within the x ray beam using fluorescence spectra recorded while the sample was translated laterally through the beam. The long axis of the strip was aligned along the beam direction, and specular x ray reflectivity data were recorded as a function of angle. Off-specular scans, offset by –0.1° in Θ, were measured and subtracted from the specular scans to remove the forward diffuse scattering and thereby obtain true specular reflectivity. The reflectivity data were normalized to the incident flux in order to compensate for variations in intensity from the radiation source as a function of time.

Fluorescence measurements were recorded at the XMaS beamline with an incident energy of 12.5 keV selected to above the Au L-edge. The fluorescence signal was recorded using a vortex Si drift diode, and the data processed with a multichannel analyzer (MCA). The penetration-depth of the x rays was varied by scanning the incident angle, Θ, between 0° and 1°. Fluorescence intensities were extracted by fitting the elemental emission peaks to a pseudo-Voigt function for each of the K edges of Ni, Fe, and Ga, as well as the L emission lines of Au. Depth information was obtained by plotting the intensity of the strongest fluorescence as a function of incidence angle for each element.[44] Incident flux normalization and a "beam footprint" correction were applied to the fluorescence data.

III. RESULTS AND DATA ANALYSIS

The true specular x ray reflectivity data for irradiated and unirradiated bilayers are shown in Fig. 1. The experimental

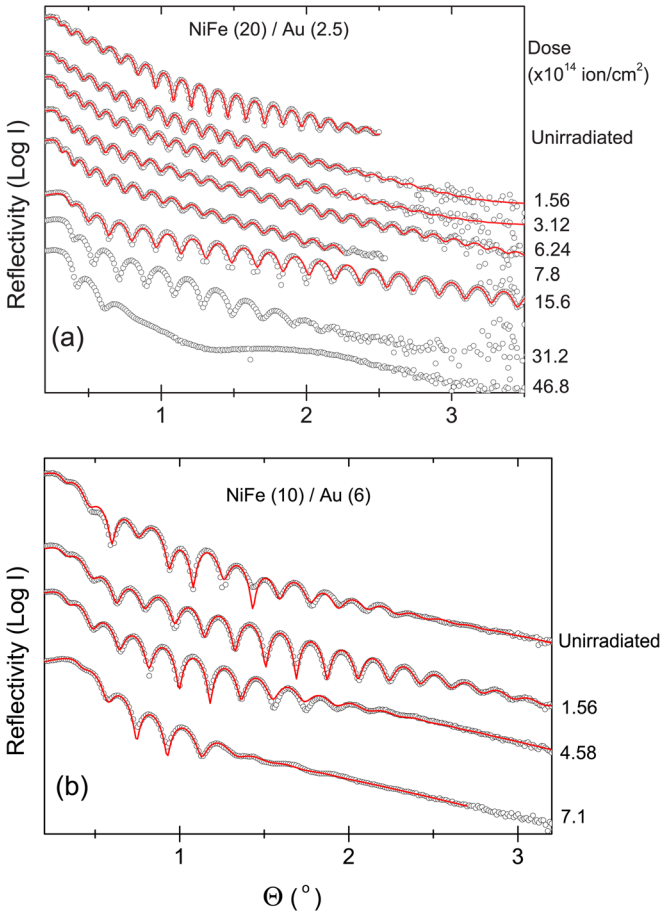

FIG. 1. (Color online) Experimental x ray reflectivity data points (circles) and corresponding best fit curves (solid lines) for different structures: (a) bilayer NiFe (20)/Au (2.5) and (b) bilayer NiFe (10)/Au (6). The curves are shifted vertically for clarity.

data were fitted using the commercial Bede REFS software.[45] The software uses a genetic algorithm to fit the measured x ray reflectivity curves by iteratively adjusting layer thickness t, mass density ρ, interface width σ, and relative layer composition x, y. For a given set of input parameters for the layers, the calculated reflectivity curve is numerically compared to the measured data and adjusted until the best fit is achieved. A limitation of specular x ray reflectivity is that the analysis cannot distinguish between topological roughness or compositional intermixing of components at an interface. Both terms contribute to the interface width parameter, σ, which is defined as the root mean square (rms) roughness at the interface and is related to the topological, σ_{topol}, and intermixing, $\sigma_{intermix}$, parameters according to[46]

$$\sigma = \sqrt{\sigma_{topol}^2 + \sigma_{intermix}^2}. \quad (1)$$

The solid lines in Fig. 1 show the best fits to the x ray data based upon the model structures with the best fitting model parameters obtained from the two bilayer systems presented in Table II. The details of the fitting models and procedure are as follows: An initial model of $SiO_2/Ni_{85}Fe_{15}/Au$ with nominal layer thicknesses and densities was created for the unirradiated bilayers (the quantitative composition of the NiFe layer was taken from the fluorescence measurements).

TABLE II. Structural models and parameters for best fits to the x ray reflectivity measurement on both samples.

Sample #	Model	Thickness (nm)	Density (% of bulk)	Interface width (nm)
1A	Au	0.21 ± 0.01	17 ± 1	0.31 ± 0.01
	Au	2.53 ± 0.05	93 ± 1	0.91 ± 0.02
	$Ni_{85}Fe_{15}$	20.5 ± 0.1	95 ± 1	0.95 ± 0.03
	SiO_2	∞	100 (fixed)	0.53 ± 0.01
2A	Au	0.31 ± 0.06	23 ± 1	0.37 ± 0.01
	Au	2.16 ± 0.21	94 ± 4	0.84 ± 0.03
	$Ni_{85}Fe_{15}$	20.2 ± 0.2	96 ± 1	2.0 ± 0.1
	$NiFe_2O_4$	0.35 ± 0.08	105 ± 1	0.49 ± 0.01
	SiO_2	∞	100	0.69 ± 0.02
3A	Au	0.71 ± 0.02	88 ± 2	0.69 ± 0.01
	$Ni_{0.5}Fe_{0.11}Au_{0.39}$	2.66 ± 0.23	94 ± 1	0.34 ± 0.01
	$Ni_{85}Fe_{15}$	18.8 ± 0.2	95 ± 1	1.88 ± 0.19
	$NiFe_2O_4$	0.6 ± 0.1	101 ± 4	0.51 ± 0.01
	SiO_2	∞	100	0.91 ± 0.05
4A	Au	0.55 ± 0.02	87 ± 1	0.59 ± 0.01
	$Ni_{0.58}Fe_{0.15}Au_{0.27}$	3.1 ± 0.1	99 ± 1	0.29 ± 0.01
	$Ni_{85}Fe_{15}$	18.0 ± 0.3	95 ± 1	2.1 ± 0.2
	$NiFe_2O_4$	0.8 ± 0.06	109 ± 4	0.42 ± 0.01
	SiO_2	∞	100	0.81 ± 0.03
5A	Au	0.4 ± 0.05	85 ± 2	0.5 ± 0.1
	$Ni_{0.56}Fe_{0.1}Au_{0.34}$	3.5 ± 0.3	78 ± 1	0.38 ± 0.01
	$Ni_{85}Fe_{15}$	17.4 ± 0.3	98 ± 1	1.7 ± 0.3
	$NiFe_2O_4$	0.9 ± 0.1	102 ± 9	0.52 ± 0.03
	SiO_2	∞	100	0.82 ± 0.06
1B	Au	0.21 ± 0.05	15 ± 2	0.27 ± 0.04
	Au	5.85 ± 0.2	90 ± 4	0.86 ± 0.01
	$Ni_{85}Fe_{15}$	10.2 ± 0.03	97 ± 2	0.67 ± 0.02
	SiO_2	∞	100 (fixed)	0.63 ± 0.01
2B	Au	5.35 ± 0.07	92 ± 1	0.49 ± 0.02
	$Ni_{85}Fe_{15}$	10.0 ± 0.1	96 ± 1	1.21 ± 0.06
	SiO_2	∞	100	0.29 ± 0.02
3B	Au	4.1 ± 0.1	88 ± 1	0.62 ± 0.01
	$Ni_{0.55}Fe_{0.1}Au_{0.35}$	2.2 ± 0.4	105 ± 4	0.58 ± 0.13
	$Ni_{85}Fe_{15}$	8.7 ± 0.4	99 ± 3	1.6 ± 0.2
	$NiFe_2O_4$	0.21	97 ± 25	0.4 ± 0.1
	SiO_2	∞	100	0.22 ± 0.06
4B	Au	4.98 ± 0.08	84 ± 1	1.12 ± 0.01
	$Ni_{0.5}Fe_{0.1}Au_{0.4}$	2.8 ± 0.3	100 ± 2	0.89 ± 0.05
	$Ni_{85}Fe_{15}$	8.6 ± 0.3	102 ± 3	2.1 ± 0.2
	$NiFe_2O_4$	0.88 ± 0.08	100 ± 5	0.41 ± 0.02
	SiO_2	∞	100	0.63 ± 0.03

For the unirradiated samples, there was good agreement between model values for the layer thicknesses and bulk densities and the nominal values of the as-grown bilayers.

For the A series bilayer irradiated with the lowest fluence (2 A), an excellent fit was obtained using the same layered structure model as for the unirradiated bilayer. The fitting indicates a decrease of the Au thickness attributed to the sputtering of Au atoms and a doubling of NiFe/Au interface width from 0.95 nm to 2.0 nm, indicating a significant intermixing of the layers has occurred for this low ion fluence. For both the unirradiated and low fluence bilayers, the best fitting model also required an additional thin, low-density Au layer on the top of the nominal gold layers for each sample. This may be attributed to surface contamination or perhaps partial surface oxidation of Au. This layer is sputtered away for higher fluences. Also, the fitting indicates the presence of an ultrathin layer of the $NiFe_2O_4$ layer at the interface between the SiO_2 and NiFe layers. This is consistent with earlier work, which showed that a transition metal layer grown adjacent to an oxide layer is partially oxidized.[47] The range of the oxidized region increases due to the intermixing for higher fluences. For bilayers irradiated with fluences above a critical fluence of 1.56×10^{14} ion/cm^2, the experimental data could not be fitted satisfactorily using the simple NiFe/Au interface. For these higher fluence values, the width of the interface region between the NiFe and the Au becomes comparable with the thickness of the upper layer and the model becomes unreliable. To model the structures exposed to higher fluences, the fitting model incorporated an additional "interfacial-intermixed" layer of $Ni_xFe_yAu_{(1-x-y)}$ between the pure NiFe and Au layers. It is recognized that this approach presents a simplified representation of the intermixed region as a layer of uniform composition, whereas, in reality, a composition gradient through this region is expected. However, this approach makes fitting tractable and allows the spatial development of intermixing and perhaps the composition and density of the intermixed region resulting from irradiation to be followed with only a few parameters. Furthermore, a similar approach has been used by other groups.[41,48–50]

The composition of the interfacial-intermixed layer was set initially at $x = 0.5$ and $y = x/5.6$ parameters estimated from the fluorescence data. Excellent fits were obtained with this model for irradiation fluences from 3.12×10^{14} up to 7.8×10^{14} ions/cm^2. The thickness of the interfacial-intermixed layer increased with fluence, indicating the increasing depth of intermixing. The thickness of the Au layer decreases due to the formation of the intermixed layer and is also reduced by sputtering. For bilayers irradiated with fluences above 7.8×10^{14} ion/cm^2, the structural model involving an interfacial-intermixed layer was no longer applicable, because the distinct Au capping layer was not present and the intermixing region extended to the surface. The experimental data for the bilayer irradiated with doses above 7.8×10^{14} ion/cm^2 were fitted without a Au layer and with a uniform $Ni_xFe_yAu_{(1-x-y)}$ layer on the top of the NiFe layer. The goodness of fit was poor in comparison to that of lower doses, and it is suggested that this is also associated with the large compositional gradient through the intermixed region. For bilayers irradiated with fluences above 31.2×10^{14} ion/cm^2, the experimental data could not be fitted with any reasonable model, and this is due to the amorphization of the crystal structure taking place.

The experimental data for the series B structures were fitted well using similar structural models to those described above. As before, the thickness of the Au layer reduces with increasing dose due to sputtering, and the thickness of the interfacial layer increases. The best fit model parameters for all of the samples are shown in Table II.

Depth-resolved x ray fluorescence measurements are complementary to the reflectivity analysis, especially when studying ion-induced intermixing. Comparing the angular

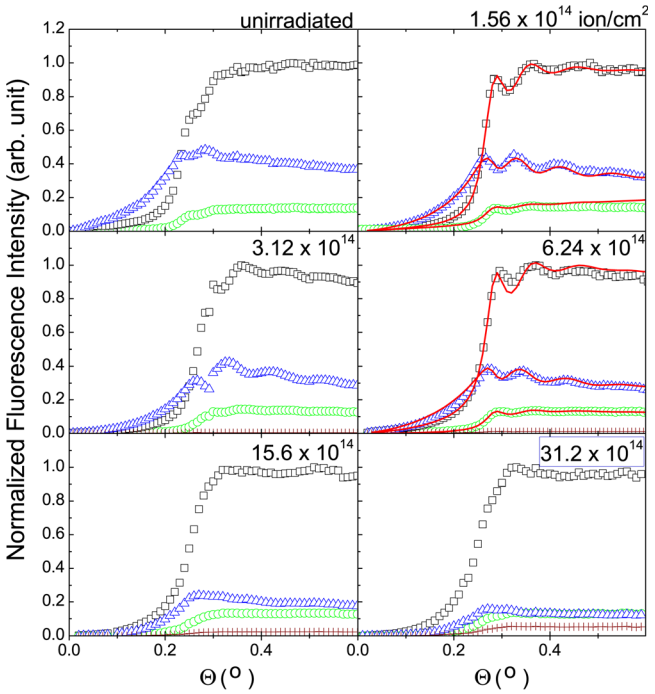

FIG. 2. (Color online) Angular dependence of the normalized fluorescence intensities of Ni (□), Fe (○), Au (Δ), and Ga^+ (+) atoms in series A samples irradiated with different fluences. The data are normalized to the corresponding Ni maximum intensity for each structure. The solid lines are fits to the fluorescence data obtained using the models and parameters shown in Table III.

dependence of the fluorescence intensities for different irradiation fluences provides valuable information about the relative replacement of the fluorescing atoms. Figure 2 shows the angular dependence of the fluorescence intensity for structures in series A. The shape of the curves are typical for thin films, a sharp arise at low angles reaching a maximum around the critical angle followed by a plateau. The spectra show oscillations due to the interference of standing waves inside the layers. The oscillations are somewhat more pronounced for Au, because standing wave effects become more significant for thinner layers. The fluorescence signal from Ga^+ becomes detectable (above the noise level) for the structure 3 A and increases for structures irradiated at higher fluences. The most significant feature in Fig. 2 is the change in the Au spectra for the different structures. The steep increase below 0.2° for structure 1 A and 2 A indicates clearly that Au is on the surface. However, as the fluence increases, the onset of Au (from the critical angle) progressively shifts toward higher angles accompanied by a decrease in the maximum amplitude, implying that the abundance of Au on the surface decreases due to the sputtering and intermixing of Au atoms, supporting the interpretation of the reflectivity data. In addition, the shape of the Au curve becomes more similar to that of Fe at higher fluences, indicating that the spatial distribution of the Au and Fe has become the same as the Au atoms migrate into the NiFe layer, forming the interfacial-mixed layer. For structure 4 A, a thin Au layer still remains on the surface, while the surface becomes Ni rich for structures 6 A and 7 A. It is important to note that the Au distribution finally gets very close to that of Fe in structure 7 A, suggesting that sample is composed of Au embedded in NiFe. The results obtained from the fluorescence measurements provide direct qualitative support for the models used to interpret the reflectivity behavior (cf. Table II). X ray fluorescence can be used to determine the layer composition much more accurately than x ray reflectivity, but quantitative analysis is complex and difficult, due to the absorption and enhancement of the fluorescence yield among all of the layers.[51,52] Nonetheless, fluorescence data has been fitted using REFS code for structures 2 A and 4 A (see solid lines in Fig. 2) to investigate the quantitative agreement between the two techniques. The fluorescence intensity is highly sensitive to chemical composition within the layers and through the interfaces. In the fitting procedure, only the density, ρ, interface widths, σ, at the NiFe/Au and intermixed layers and the x and y parameters were allowed to vary. All the remaining parameters were kept identical to those found from fitting the reflectivity data. This gives a more straightforward comparison between the two techniques and also more reliable fitting of fluorescence data, as the number of the fitting parameters are fewer. Excellent fits were obtained and the parameters extracted from the fluorescence fitting are shown in Table III. The parameters for structure 1 A are close to those obtained from fitting the reflectivity data (cf. Table II). The densities obtained from the two techniques differ by less than 10% and are in reasonable agreement. Furthermore, the interface widths are almost identical, except for the Au layer. For structure 4 A, the density parameters are associated with large error bars. This is because the intermixing becomes effective and the density gradient between the layers is enhanced; plus, the implanted Ga^+ may make the density gradient more complex. Despite the complexity of the physical process, the fits to the ADXRF give similar parameters to those obtained from fitting the reflectivity, and in particular, the agreement in the chemical and structural parameters for the interfacial-intermixed layer is significant.

The path of the implanted Ga^+ ions was tracked as a function of the irradiation fluence by ADXRF measurement in our samples. Ga^+ fluorescence intensity (normalized to Ni ($\Phi = 31.2 \times 10^{14}$ ion/cm^2)) from structures 4 A ($\Phi = 6.24 \times 10^{14}$ ion/cm^2) and 7 A ($\Phi = 31.2 \times 10^{14}$ ion/cm^2) are shown in Fig. 3(a). For structure 4 A, the sharp increase at low angles indicates that implanted ions are located close to

TABLE III. Density and interface width parameters extracted from fits to the fluorescence data for structures 2A and 4A. Thickness, density, and interface width of SiO_2 and $NiFe_2O_4$ layers were kept to those used to fit the reflectivity measurements. The density and interface widths of Au, NiFe, and intermixed layers were the only free fitting parameters.

Sample #	Layers	Density (% of bulk)	Interface width (nm)
2A	Au	15 ± 9	0.35
	Au	104 ± 3	1.8
	$Ni_{85}Fe_{15}$	90 ± 2	2.1
4A	Au	80 ± 48	0.5
	$Ni_{0.5}Fe_{0.12}Au_{0.38}$	107 ± 18	0.4
	$Ni_{82}Fe_{17}$	90 ± 14	2.4

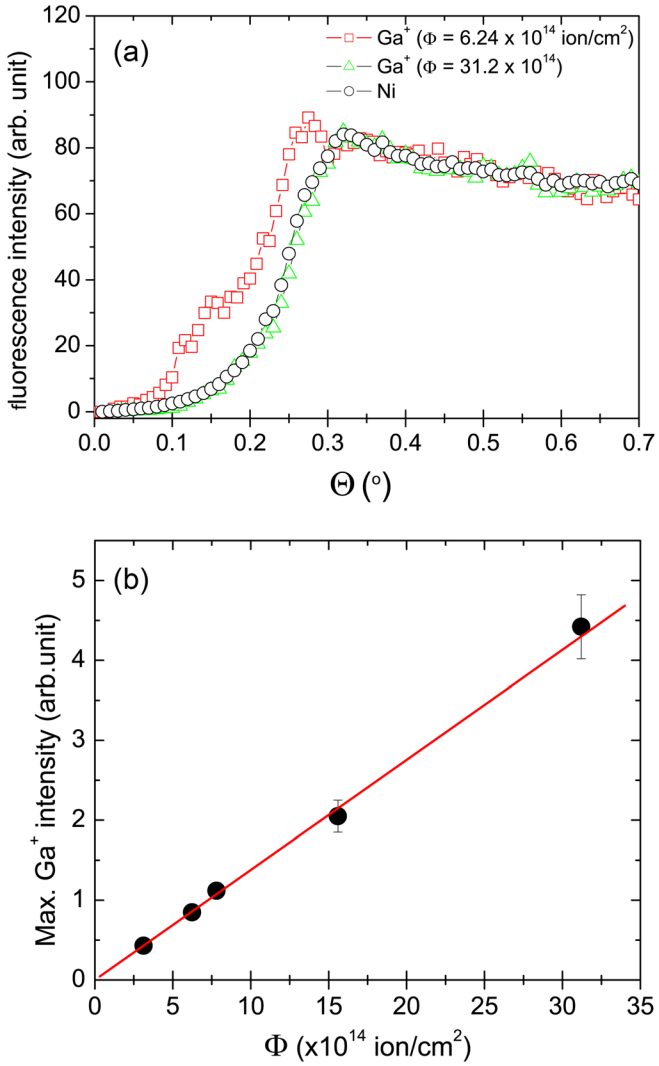

FIG. 3. (Color online) (a) Measured Ga^+ fluorescence intensities for $\phi = 6.24 \times 10^{14}$ (□) and 31.2×10^{14} ion/cm^2 (Δ) normalized with respect to the Ni (○). (b) The maximum amplitude of the Ga^+ fluorescence intensity, which corresponds to amount of implanted Ga^+ ions as a function of irradiation fluence. The solid line is a linear fit to the data points.

the surface, while for 7 A, the Ga^+ fluorescence intensity follows almost identically that of Ni, indicating that the implanted ions are embedded in the NiFe layer throughout the sample. It shows that, as the irradiation fluence increases, more Ga^+ ions penetrate deeper into the sample. Furthermore, since the fluorescence intensity maximum is proportional to the quantity of the corresponding atomic species, the accumulation of Ga^+ as a function of fluence can be compared between the simulations and experiments, as shown in Fig. 3(b), where the linear fit shows the strong correlation between the Monte Carlo simulations and the fluorescence data. The simulations and energy dispersive x ray measurements showed that the maximum atomic Ga^+ content is less than 1% for fluences $\Phi < 15.6 \times 10^{14}$ (low dose regime). Corb *et al.*[53,54] studied chemical bonding, magnetic moments, and local symmetry in transition metal-metalloid alloys and suggested that the magnetic moment of a Ni-Ga alloy will reach zero with the addition of 20 at. % of Ga^+. Also, Ikeda *et al.*[55] reported that a single-phase region exists up to about 30 at. % Ga^+ in Fe-Ga systems. Therefore, the influence of Ga^+ implantation in this dose range is expected to be negligible.

Another important aspect of the FIB irradiation is sputtering of surface atoms. Reflectivity and fluorescence measurements show the reduction in the thickness of the top layer, even at the lowest dose. We calculated the number of NiFe and Au atoms in each NiFe (20)/Au (2.5) bilayer structure using the reflectivity fit parameters and plotted this as a function of fluence in Fig. 4(a). The total amount of NiFe atoms remains constant until $\Phi = 6.24 \times 10^{14}$ ion/cm^2 due to the very small sputtering yields of 0.018 Ni atoms/ion and 0.044 Fe atoms/ion, which resulted in only 0.01% sputtering of the NiFe. However, beyond this fluence, sputtering of NiFe atoms becomes visible as the thickness of the top Au layer is significantly reduced and the sputtering yields of Ni and Fe increase. Around 10% of the NiFe atoms are sputtered at $\Phi = 15.6 \times 10^{14}$ ion/cm^2 as shown in Fig. 4(a). In comparison, the amount of Au falls systematically down to 35% due to sputtering. These experimental results are predicted by SRIM[56] calculations SRIM calculations, shown

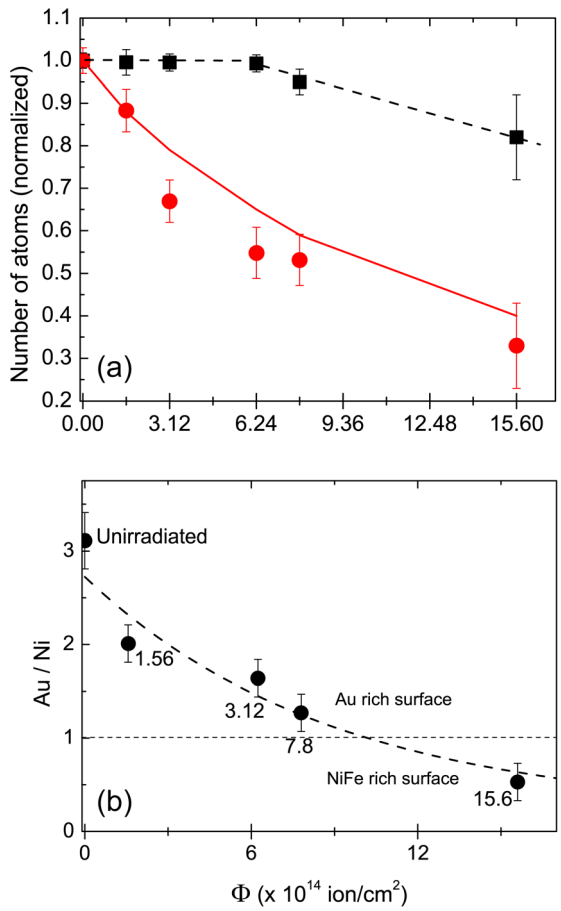

FIG. 4. (Color online) (a) The number of NiFe ■ and Au ● atoms as a function of fluence for the series A samples. Data are normalized to the corresponding number of atoms in the unirradiated strip. The data points are calculated using t, ρ, x, and y parameters tabulated in Table II, and the solid line is the result of calculations derived from the Monte Carlo simulations. (b) The Au/Ni intensity ratio as a function of fluence for the same bilayer series. Intensity ratios were calculated at a glancing angle $\Theta_c(Ni) - 0.05°$ for each strip using the fluorescence curves shown in Fig. 2. (Dashed lines are guide to eyes).

as solid lines in Fig. 4(a), using the sputtering yields given above, although the rate of Au sputtering is somewhat underestimated; this could be due to the fact that simulations are based on the ballistic model and ignore temperature effects. Similar results were also obtained from x ray fluorescence measurements, where quantitative changes were obtained from the ratio of Au to the Ni fluorescence as a function of fluence. Figure 4(b) shows the Au/Ni intensity ratio taken at $\Theta_c(Ni) - 0.05°$, which corresponds to the relative elemental ratio in the surface region. Irradiation leads to a steady decrease of Au with increasing fluence in the low-dose regime, in which the surface remains Au rich, and in the high dose regime, the surface becomes Ni, since the surface Au atoms have been sputtered away and any remaining Au atoms are inter-mixed with the Ni and Fe, a result that is in agreement with the reflectivity results.

IV. DISCUSSION

The focused ion fluence increases both the diffusion length and the quantity of intermixed atoms, broadening the width of the bilayer interface. At high doses, sputtering and displacement of atoms-caused effects dominates structural modifications. Simulations reveal that 54% of NiFe atoms are displaced from their initial lattice sites, creating vacancies and undergoing subsequent collisions at the highest doses. Consequently, amorphisation of the layered structure and large local deviations in the chemical composition are expected for the bilayers irradiated with $\Phi > 15.6 \times 10^{14}$ ion/cm^2 (high-dose regime). These severe changes explain why the reflectivity data for bilayers irradiated with high doses could not be fitted using the layered models that were applicable at lower doses. Severe damage of the bilayers irradiated with high doses was confirmed by SEM images (not shown here). The interfacial structure within bilayer and multilayer systems is often critical to the functionality of the system. The interfacial mixing behavior has been followed for different doses using the interface width parameter, σ, deduced from the fits to the x ray reflectivity data. For series A and B bilayers irradiated with fluences $\Phi \leq 1.56 \times 10^{14}$ ion/cm^2, the interface width parameter is simply the interface roughness between the NiFe and Au layers. However, as described earlier for fluences between 1.56×10^{14}-7.8×10^{14} ion/cm^2, an interfacial-intermixed layer with its own refractive index was incorporated into the fitting model.

In order to study the focused ion beam–induced intermixing effect at the NiFe/Au interface, the total intermixing length, X, was defined as the total interface width, σ, between the NiFe(Au) and Au layers plus the thickness of the interfacial-intermixed layer when present.[49,50,57] The kinetics of intermixing are characterized by the irradiation dose dependence of the intermixing length squared, X^2, according to the "compound formation model".[58,59] On this basis, Fig. 5 shows the experimentally derived X^2 as a function of the irradiation fluence in the low dose regime for both series of samples (the initial intermixing occurring during the growth, $X^2(0)$, has been subtracted from all the data points). For both samples, X^2 increases linearly with ion beam fluence. The behavior of X^2 with irradiation fluence

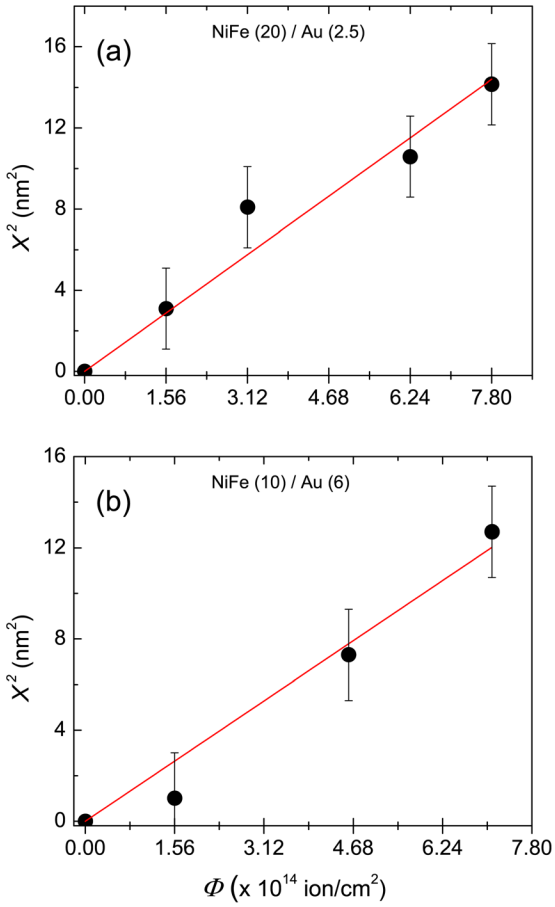

FIG. 5. (Color online) The squared intermixing length as a function of irradiation fluence for both series of samples. The linear increase indicates that the intermixing is diffusion controlled. Solid lines are linear fits to the data points.

describes the mixing process, which can be either a chemical reaction or a diffusion-controlled process. A linear dependence ($X^2 \propto \phi$) is interpreted as the diffusion controlled regime, whereas a quadratic dependence ($X^2 \propto \Phi^2$) would be expected for a chemical reaction–controlled process. Thus, our results suggest that the focused Ga^+ ion beam–induced intermixing is a diffusion-controlled process in the NiFe/Au bilayer systems studied here.

The slopes of the linear fits in Fig. 5 provide the mixing rate, $k = X^2/\Phi$, which can be used to determine the mixing type. The experimental mixing rates were found to be the same within error for the two series of samples 1.8 ± 0.1 nm^4 and 1.7 ± 0.1 nm^4 for samples A and B series, respectively. Atomic diffusion can be described by two different models, namely, the ballistic and the thermal spike model. The former considers only ballistic properties, i.e., the atomic number of the ions and target as well as the energy deposited by collisions.[60] The thermal spike model takes into account the thermodynamic properties of solids, such as the heat of mixing, ΔH_{mix}, and cohesive energy, ΔH_{coh}.[61] The theoretical mixing rate was calculated using the ballistic model according to[60]

$$k_{ball.} = \left(\frac{X^2}{\Phi}\right)_{ball.} = \frac{1}{3}\Gamma_0 \xi R_c^2 \frac{F_D}{N E_d}, \qquad (2)$$

where $\Gamma_0 = 0.608$ is a constant, $R_c = 1$ nm is the minimum separation distance for a stable Frenckel pair, $\xi = 2(m_1 m_2)^{1/2}/(m_1 + m_2)$, where m_1 is the mass of the ion and m_2 the average mass of the target atoms, N is the average atomic density of the target, $E_d = 25$ eV is the displacement energy, and F_D is the deposited energy density at the interface taken from the SRIM simulations. The theoretical ballistic mixing rate for the A and B series under the given experimental conditions are deduced as 0.27 nm^4 and 0.23 nm^4, respectively. These are an order of magnitude smaller than those found experimentally. This clearly shows that the mechanism of focused ion beam–induced intermixing is not ballistic and thermodynamical factors should be taken into account in this system. FIB-specific features might play an important role in the nature of the intermixing process compared to that of conventional techniques. The beam diameter varies between 0.2 and 1.0 mm in conventional techniques, whereas it is in the range of 0.01-1 μm (0.1 μm in our experiments); also fast-rastering speed of 1 μs is much smaller than the long irradiation time employed in conventional techniques. The significant contrast in the parameters between FIB may cause highly localized kinetic energy transfer, possible heating, as well as head and matter deposition at the target, which, in turn, may lead to differences in the intermixing process.

V. CONCLUSION

A series of NiFe (20 nm)/Au (2.5 nm) and NiFe (10 nm)/Au (6 nm) bilayer structures were irradiated with a focused Ga^+ ion beam. The structural and compositional effects on the bilayers were studied as a function of irradiation dose. GIXRR and ADXRF analysis supported by Monte Carlo simulations identify two distinct irradiation regimes, namely, low dose ($1.56 \times 10^{14} < \Phi < 15.6 \times 10^{14}$ ion/cm^2) and high dose ($\Phi > 15.6 \times 10^{14}$ ion/cm^2) regimes. In the latter, sputtering and ion implantation effects were found to be dominant, causing amorphization of the bilayer structures at the highest high doses. In the low dose regime, the formation of an interfacial-intermixed layer between the NiFe and Au layers was demonstrated by x ray reflectivity and x ray fluorescence measurements. The consistency in the structural information obtained from high-resolution grazing-incidence x ray reflectivity and fluorescence technique supported with theoretical calculations highlights the functionality of the combined GIXRR and ADXRF techniques in identifying the formation of nanoscale interfaces. The formation of this $Ni_{x}Fe_{y}Au_{1-x-y}$ layer occurs at a critical fluence of 3.24×10^{14} ion/cm^2, and its thickness increases with increasing irradiation dose. Detailed information on the mixing process was derived from the compound formation model, and it was shown that focused ion beam–induced mixing in NiFe/Au bi-layers is a diffusion controlled process. Mixing rate for both series of bilayers were found experimentally to be 1.8 nm^4 and 1.7 nm^4, and comparison to theoretical calculations using ballistics shows that thermal properties play an important role in FIB-induced mixing. Finally, as FIB irradiation is becoming a widely used technique for local patterning and modification of materials with feature sizes down to the nanoscale, and since little structural work has been done to understand the physical basis of the structural changes resulting from FIB irradiation, our study provides valuable information to understand structural and compositional changes induced by focused ion beam irradiation.

ACKNOWLEDGMENTS

This research was funded by a UK EPSRC Grant Ref. EP/G010897/1. Work on XMaS is supported through EPSRC. The authors would like to thank Laurence Bouchenoire and Stuart Wilkins for assistance with x ray measurements. Use of the National Synchrotron Light Source, Brookhaven National Laboratory, was supported by the U.S. Department of Energy, Office of Science, Office of Basic Energy Sciences, under Contract No. DE-AC02-98CH10886.

[1]D. Atkinson, D. A. Allwood, G. Xiong, M. D. Cooke, C. C. Faulkner, and R. P. Cowburn, Nature Mater. **2**, 85 (2003).
[2]D. A. Allwood, G. Xiong, C. C. Faulkner, D. Atkinson, D. Petit, and R. P. Cowburn, Science **309**, 1688 (2005).
[3]J. Lohau, A. Moser, C. T. Rettner, M. E. Best, and B. D. Terris, Appl. Phys. Lett. **78**, 990 (2001).
[4]Y. Kim, A. Danner, J. Raftery, and K. Choquette, IEEE J. Sel. Top. Quantum Electron. **11**, 1292 (2005).
[5]A. Stanishevsky, S. Aggarwal, and A. S. Prakash, J. Vac. Sci. Technol. B **16**, 3899 (1998).
[6]N. W. Liu, A. Datta, C. Y. Liu, and Y. L. Wang, Appl. Phys. Lett. **82**, 1281 (2003).
[7]F. Machalett, K. Edinger, J. Melngailis, M. Diegel, K. Steenbeck, and E. Steinbeiss, Appl. Phys. A: Mater. Sci. Process. **71**, 331 (2000).
[8]D. McGrouther and J. N. Chapman, Appl. Phys. Lett. **87**, 022507 (2005).
[9]P. Warin, R. Hyndman, J. Glerak, J. N. Chapman, J. Ferre, J. P. Jamet, V. Mathet, and C. Chappert, J. Appl. Phys. **90**, 3850 (2001).
[10]C. C. Faulkner, D. Atkinson, D. A. Allwood, and R. P. Cowburn, J. Magn. Magn. Mater. **319**, 9 (2007).
[11]R. Hyndman, P. Warin, J. Gierak, J. Ferre, J. N. Chapman, J. P. Jamet, V. Mathet, and C. Chappert, J. Appl. Phys. **90**, 3843 (2001).
[12]W. M. Kaminsky, G. A. C. Jones, N. K. Patel, W. E. Booij, M. G. Blamire, S. M. Gardiner, Y. B. Xu, and J. A. C. Bland, Appl. Phys. Lett. **78**, 1589 (2001).
[13]A. Aziz, S. J. Bending, H. G. Roberts, S. Crampin, P. J. Heard, and C. H. Marrows, Phys. Rev. Lett. **97**, 206602 (2006).
[14]R. Lavrijsen, J. H. Franken, J. T. Kohlhepp, H. J. M. Swagten, and B. Koopmans, Appl. Phys. Lett. **96**, 222502 (2010).
[15]C.-M. Park and J. A. Bain, J. Appl. Phys. **91**, 6830 (2002).
[16]D. McGrouther, J. Chapman, and F. Vanhelmont, J. Appl. Phys. **95**, 7772 (2004).
[17]A. Barna, L. Kotis, J. L. Labar, Z. Osvath, A. L. Toth, M. Menyhard, A. Zalar, and P. Panjan, J. Appl. Phys. **102**, 053513 (2007).
[18]M. Hitzfeld, P. Ziemann, W. Buckel, and H. Claus, Phys. Rev. B **29**, 5023 (1984).
[19]M. Hitzfeld and P. Ziemann, Phys. Rev. B **32**, 3026 (1985).
[20]C. Chappert, Science **280**, 1919 (1998).
[21]B. D. Terris, L. Folks, D. Weller, J. E. E. Baglin, A. J. Kellock, H. Rothuizen, and P. Vettiger, Appl. Phys. Lett. **75**, 403 (1999).
[22]D. Ravelosona, C. Chappert, V. Mathet, and H. Bernas, Appl. Phys. Lett. **76**, 236 (2000).
[23]L. Folks, R. E. Fontana, B. A. Gurney, J. R. Childress, S. Maat, J. A. Katine, J. E. E. Baglin, and A. J. Kellock, J. Phys. D: Appl. Phys. **36**, 2601 (2003).
[24]V. Dasgupta, N. Litombe, W. E. Bailey, and H. Bakhru, J. Appl. Phys. **99**, 08G312 (2006).
[25]C. Vieu, J. Gierak, H. Launois, and T. Aign, J. Appl. Phys. **91**, 3103 (2002).
[26]T. Devolder, J. Ferré, C. Chappert, H. Bernas, J.-P. Jamet, and V. Mathet, Phys. Rev. B **64**, 064415 (2001).
[27]K. Zhang, K. Lieb, M. Marszalek, V. Milinovic, and V. Tokman, Thin Solid Films **515**, 700 (2006).
[28]T. Devolder, Phys. Rev. B **62**, 5794 (2000).

[29]S. I. Woods, S. Ingvarsson, J. R. Kirtley, H. F. Hamann, and R. H. Koch, Appl. Phys. Lett. **81**, 1267 (2002).
[30]J. Ferre, C. Chappert, H. Bernas, J. Jamet, P. Meyer, O. Kaitasov, S. Lemerle, V. Mathet, F. Rousseaux, and H. Launois, J. Magn. Magn. Mater. **198**, 191 (1999).
[31]J. Fassbender, D. Ravelosona, and Y. Samson, J. Phys. D: Appl. Phys. **37**, R179 (2004).
[32]C. T. Rettner, S. Anders, J. E. E. Baglin, T. Thomson, and B. D. Terris, Appl. Phys. Lett. **80**, 279 (2002).
[33]J. Jaworowicz, A. Maziewski, P. Mazalski, M. Kisielewski, I. Sveklo, M. Tekielak, V. Zablotskii, J. Ferre, N. Vernier, A. Mougin, A. Henschke, and J. Fassbender, Appl. Phys. Lett. **95**, 022502 (2009).
[34]M. J. Bonder, N. D. Telling, P. J. Grundy, C. A. Faunce, T. Shen, and V. M. Vishnyakov, J. Appl. Phys. **93**, 7226 (2003).
[35]T. Blon, G. Ben Assayag, J. Ousset, B. Pecassou, A. Claverie, and E. Snoeck, Nucl. Instrum. Methods Phys. Res. B **257**, 374 (2007).
[36]D. Weller, J. E. E. Baglin, A. J. Kellock, K. A. Hannibal, M. F. Toney, G. Kusinski, S. Lang, L. Folks, M. E. Best, and B. D. Terris, J. Appl. Phys. **87**, 5768 (2000).
[37]J. Fassbender and J. McCord, Appl. Phys. Lett. **88**, 252501 (2006).
[38]J. Fassbender, J. von Borany, A. Mücklich, K. Potzger, W. Möller, J. McCord, L. Schultz, and R. Mattheis, Phys. Rev. B **73**, 184410 (2006).
[39]J. Fassbender, A. Mucklich, K. Potzger, and W. Moller, Nucl. Instrum. Methods Phys. Res. B **248**, 343 (2006).
[40]V. Sisodia, D. Kabiraj, W. Bolse, and I. Jain, Appl. Surf. Sci. **252**, 4016 (2006).
[41]M. G. Le Boitie, A. Traverse, L. Nevot, B. Pardo, and J. Corno, Nucl. Instrum. Methods Phys. Res. **29**, 653 (1988).
[42]S. Amirthapandian, B. Panigrahi, A. Srivastava, S. Dhara, A. Gupta, V. Sastry, R. Nandedkar, K. Nair, and A. Narayanasamy, J. Appl. Phys. **95**, 5295 (2004).
[43]L. Bogart, "An investigation of the structure, pinning and magnetoresistance of domain walls in $Ni_{81}Fe_{19}$ planar nanowires," Ph.D. dissertation (Durham University, 2010).
[44]T. P. A. Hase, B. K. Tanner, P. Ryan, C. H. Marrows, and B. J. Hickey, IEEE Trans. Magn. **34**, 831 (1998).
[45]*REFS Reflectivity Simulation Software* (Bede Scientific Instruments, Lindsey Park, Durham, UK, 1996).
[46]M. Wormington, I. Pape, T. P. A. Hase, B. K. Tanner, and D. K. Bowen, Philos. Mag. Lett. **74**, 211 (1996).
[47]T. J. Regan, H. Ohldag, C. Stamm, F. Nolting, J. Luning, J. Stöhr, and R. L. White, Phys. Rev. B **64**, 214422 (2001).
[48]M. Nayak, G. S. Lodha, and R. V. Nandedkar, Bull. Mater. Sci. **29**, 693 (2006).
[49]A. Traverse, M. Le Boite, L. Nevot, B. Pardo, and J. Corno, Appl. Phys. Lett. **51**, 1901 (1987).
[50]J. D. R. Buchanan, T. P. A. Hase, B. K. Tanner, P. J. Chen, L. Gan, C. J. Powell, and W. F. Egelhoff, Jr., Phys. Rev. B **66**, 104427 (2002).
[51]D. De Boer, Spectrochim. Acta, Part B **46**, 1433 (1991).
[52]T. Huang and W. Lee, Anal. Sci. **11**, 529 (1995).
[53]B. Corb, R. O'Handley, and N. Grant, Phys. Rev. B **27**, 636 (1983).
[54]B. Corb, Phys. Rev. B **31**, 2521 (1985).
[55]O. Ikeda, R. Kainuma, I. Ohnuma, K. Fukamichi, K. Ishida, R. Kainuma, I. Ohnuma, K. Fukamichi, and K. Ishida, J. Alloys Compd. **347**, 198 (2002).
[56]J. F. Ziegler, M. D. Ziegler, and J. P. Biersack, Nucl. Instrum. Methods Physics Res. B **268**, 1818 (2010).
[57]W. Priyantha, H. Chen, M. Kopczyk, R. J. Smith, A. Kayani, A. Comouth, M. Finsterbusch, P. Nachimuthu, and D. McCready, J. Appl. Phys. **103**, 014508 (2008).
[58]J. Desimoni and A. Traverse, Phys. Rev. B **48**, 13266 (1993).
[59]S. Dhar, Y. N. Mohapatra, and V. N. Kulkarni, Phys. Rev. B **54**, 5769 (1996).
[60]P. Sigmund and A. Gras-Marti, Nucl. Instrum. Methods **182**, 25 (1981).
[61]W. Bolse, Mater. Sci. Eng. R **12**, 53 (1994).